Journal of Environmental Chemical Engineering 10 (2022) 107955

Contents lists available at ScienceDirect

Journal of Environmental Chemical Engineering

journal homepage: www.elsevier.com/locate/jece

Photoelectrocatalytic degradation of pharmaceuticals and inactivation of viruses in water with tungsten oxide electrodes

A. Tolosana-Moranchel [a,*], N. Pichel [b], H. Lubarsky [a], J.A. Byrne [a], P. Fernández-Ibañez [a,*]

[a] Nanotechnology and Integrated BioEngineering Centre, School of Engineering, Ulster University, Northern Ireland BT37 0QB, UK
[b] CIESOL, Joint Centre University of Almeria-CIEMAT, Almeria, Spain

ARTICLE INFO

Editor: Despo Kassinos

Keywords:
Photoelectrocatalysis
Contaminant of emerging concern
Bacteriophage
WO_3
Photoanode
Water disinfection

ABSTRACT

Electrochemically assisted photocatalysis (EAP) is one approach to overcome the fast recombination rates in photocatalysis and increase the quantum efficiency to produce ROS. In comparison to TiO_2, tungsten trioxide (WO_3) can utilize UV and visible photons and with EAP the external bias can be used to drive the reduction pathway. In this work WO_3 electrodes were prepared hydrothermally on FTO. Vertically grown WO_3 nanoplate-like structures were thoroughly characterized. The WO_3 photoanodes improved photocurrent response compared to P25 and a visible response was measured. These results were attributed to smaller charge transfer resistance and their morphology. The activity of the photoanodes was assessed on the EAP degradation of sulfamethoxazole and MS2 bacteriophage. WO_3 yielded ten times higher degradation rates for sulfamethoxazole ($2.21 \cdot 10^{-6}$ mmol cm^{-2} min^{-1}) compared to P25. WO_3 also yielded the fastest MS2 inactivation rate. A rapid 5-log removal was achieved in 6 min with WO_3 that maintained activity over 5 cycles.

1. Introduction

Contaminants of Emerging Concern (CECs) include a wide range of chemicals such as pharmaceutical, pesticides, personal care products, food additives or hormones, mainly originated from human wastes and industrial effluents. There is increasing concern about the release of pharmaceuticals as they have been detected in various water matrices at low concentrations (μg L^{-1} or ng L^{-1}) [1,2]. Furthermore, the release of antibiotics can contribute to the rise in antibiotic resistant bacteria (ARB) and antibiotic resistance genes (ARGs), posing a global threat to human health [3]. Due to the continuous presence of viruses in wastewater and the recent COVID-19 (SARS-CoV-2) pandemic there is increasing concern about the transmission of viral pathogens [4,5]. Transmission of the virus via the fecal-oral pathway can lead to virus-infected wastewater transported to wastewater treatment plants (WWTPs). The release of untreated water (capable to infect WWTPs workers if bioaerosols are produced), pollution of surface water and land-application of residual biosolids produced in the WWTPs can act as secondary source of viral transmission [5]. The likelihood of viral transmission is higher in countries with poor access to sanitation. Even though studies have shown high efficiencies of anaerobic sludge treatment for virus reduction, it is necessary to upgrade existing WWTPs to include tertiary treatment [4]. Furthermore, conventional wastewater treatments are not effective for the removal of CECs but Advanced Oxidation Processes (AOPs) have emerged as a potential solution [6]. TiO_2-photocatalysis, based on the generation Reactive Oxygen Species (ROS) is an alternative novel and effective approach to degrade organic pollutants and inactivate disinfection resistant microorganisms [7]. However, TiO_2 is active only under UV radiation (wavelengths below ca. 400 nm) and therefore the solar efficiency is limited and it presents low quantum efficiencies due to fast charge carrier recombination [8]. The solar efficiency can be improved by using alternative photocatalysts with narrower band gaps or by modification of the parent material to improve achieve visible light absorption [9]. WO_3 has been investigated

Abbreviations: CEC, Contaminants of Emerging Concern; ARB, Antibiotic Resistant Bacteria; ARG, Antibiotic Resistance Genes; WWTP, Wastewater Treatment Plant; AOP, Advanced Oxidation Processes; ROS, Reactive Oxygen Species; EAP, Electrochemically Assisted Photocatalysis; OTE, Transparent Supporting Electrode; TCO, Transparent Conductive Oxides; FTO, Fluorine Doped Tin Oxide; ITO, Indium Doped Tin Oxide; SEM, Scanning Electron Microscopy; EDX, Dispersive Energy X-Ray; SCE, Saturated Calomel Electrode; RHE, Reversible Hydrogen Electrode; LSV, Linear Sweep Voltammetry; ICPE, Incident Photon-to-Current Efficiency; EIS, Electrochemical Impedance Spectroscopy; E_{FB}, Flat-Band Potentials; SMX, Sulfamethoxazole; PBS, Phosphate Borate Saline; TSB, Tryptone Soya Broth; TSA, Tryptone Soya Agar; EQE, External Quantum Efficiency; APCE, Absorbed Photon to Current conversion Efficiency.

* Corresponding authors.
E-mail addresses: a.tolosana@ulster.ac.uk (A. Tolosana-Moranchel), p.fernandez@ulster.ac.uk (P. Fernández-Ibañez).

https://doi.org/10.1016/j.jece.2022.107955
Received 9 April 2022; Received in revised form 10 May 2022; Accepted 19 May 2022
Available online 24 May 2022

as an alternative to TiO_2, owing to its high stability, resistance to photocorrosion, high conductivity, and its narrower band bap extending into the visible region of the solar spectrum. The valence band edge potential of WO_3 is positive enough to oxidize water to generate hydroxyl radicals [9–11]. Electrochemically assisted photocatalysis (EAP) avoids recombination of electron-hole pairs where the external electric field drives charge carrier separation. Photogenerated valence band holes oxidize water to produce hydroxyl radicals or may directly oxidize adsorbed pollutants. Conduction band electrons are transferred via an external circuit to the counter electrode where reduction reactions take place. The external bias overcomes any limitation in the conduction band edge potential of the semiconductor to drive the reduction reactions. Among the different materials, nanostructured photocatalysts with different morphologies, from zero to one, two and three-dimensional have been reported [12]. Good degradation rates of organic compounds and inactivation of bacteria have been reported with nanostructured photocatalysts, especially TiO_2 nanotubes [13,14]. TiO_2 nanorods and nanowires have also exhibited degradation rates two times higher than P25 [15], since these 1-dimensional nanostructures can provide a "high-speed" pathway along the longitudinal direction for single-crystalline nanostructures and shorten the charge diffusion length [12].

WO_3 nanoplates and nanosheets have been investigated as semiconductor electrodes as they provide high photocurrents [16–18]. This is due to the fact that 2-dimensional nanostructures can expose highly reactive facets and shorten the charge diffusion length [19,20]. Most of these nanostructures have been prepared on non-transparent metal substrates by anodization, such as Ti or W mesh or plates [13,16].

Non-transparent conducting support electrodes allows only front-face irradiation of the electrode and the irradiation will be attenuated by the water matrix [21]. If one uses an optically transparent supporting electrode (OTE), the semiconductor can be back-face irradiated removing any loss of incident radiation due to the water matrix. The use of Transparent Conductive Oxides (TCO), such as Fluorine doped Tin Oxide (FTO) or Indium doped Tin Oxide (ITO) thin films on glass is well known [22]. They have relatively high electrical conductivity and can transmit irradiation from the visible into the UVB region. To prepare nanostructured photocatalysts on OTEs several strategies have been reported. For example, preparing TiO_2 nanotubes by anodization of metal substrates that are later attached to a transparent substrate [23] or by anodizing thin metal films sputtered on OTE surfaces [24–26]. However, these methods have only been carried out at laboratory scale and they are more complicated than other methodologies to prepare photoanodes. Hydrothermal synthesis is a relatively straightforward approach to obtaining nanostructured photocatalysts with different morphologies [12,17,27–29].

Hydrothermal synthesis of WO_3 has been reported previously using seed layers prior to performing the hydrothermal process [18], but the prepared photoanodes were not used for water treatment [20,29–31]. In this work, WO_3 was hydrothermally grown on FTO and their activity was compared with P25 nanoparticulate electrodes for the electrochemically assisted photocatalytic degradation sulfamethoxazole and the inactivation of the viral surrogate, MS2 bacteriophage. We believe this is the first report of rapid viral inactivation by EAP on WO_3 electrodes.

2. Experimental section

2.1. Materials

All the chemicals used in this study were analytical grade and used as received. Acetonitrile (Sigma-Aldrich, $CH_3CN > 99.9\%$), P25 Aeroxide® (Evonik Company), sodium tungstate dehydrate (Sigma-Aldrich, $Na_2WO_4{\cdot}2H_2O > 99\%$), formic acid (Merk, HCOOH > 98%), hydrochloric acid (Merk, HCl 37%), FTO glass (Sigma-Aldrich, fluorine-doped tin oxide SnO_2:F ~ 7 Ω/sq), methanol (Sigma-Aldrich, $CH_3OH >$ 99.9%), sodium sulfate (Sigma-Aldrich, $Na_2SO_4 > 99\%$), sodium oxalate (Aldrich, $Na_2C_2O_4 > 99.5\%$), SU8 photoresist (Microchem) and Decon™ Decon 90 (Decon Laboratories Ltd.). Deionized water (15 MΩ cm^{-1}) was used to prepare all the solutions.

2.2. Preparation of photoanodes

2.2.1. Preparation of WO_3 photoanode

FTO glass coupons (2 × 1.5 cm^2) were cleaned by sonication in Decon 90 solution, followed by rinsing in ultrapure water. WO_3 was synthesized hydrothermally as reported previously [20]. In brief, 0.231 g of sodium tungsten dehydrate ($Na_2WO_4{\cdot}H_2O$) was dissolved in ultrapure water (30 mL) under constant stirring at room temperature. Then, 10 mL of 3 M HCl were added drop by drop, followed by the addition of 0.20 g of sodium oxalate (Na_2C_2O4). After stirring for several minutes, more ultrapure water was added to get a total volume of 70 mL solution which was stirred for 30 min. The solution and FTO glass were then transferred into a Teflon-lined stainless Parr reactor (80 mL). The hydrothermal synthesis was carried out at two different synthesis conditions: 180 °C for 3 h and 120 °C for 12 h (from here on out named as WO_3 180 °C 3 h and WO_3 120 °C 12 h). The FTO substrate was washed with ultrapure water and dried at 60 °C overnight. The as-prepared samples were calcined in air at 450 °C for 1 h with a heating up and cooling down ramps of 2 °C min^{-1}. Electrical contacts were made by attaching a copper wire to an uncoated area of the conductive face of the FTO using silver epoxy. The contact, wire and the uncoated area of the conductive face of the FTO were insulated using a negative photoresist (NANO™ SU-8, Microchem) which was cured under UV-B exposure for 15 min and hard baked at 160 °C for 20 min.

2.2.2. Preparation of P25 photoanode

A suspension of P25 in methanol (25 g L^{-1}) was sonicated for 15 min. After cleaning the FTO coupons, they were put on a hot plate at 60 °C and spray coated with the P25 suspension using an airbrush gun with intermittent weighing. The FTO was coated until the desired weight was reached (1 mg cm^{-2}). This loading was previously reported to give optimal performance in the photocatalytic and electrochemically assisted photocatalytic oxidation of formic acid and atrazine [32,33]. The coated coupons were annealed in air at 450 °C for 1 h with a heating up and cooling down ramps of 2 °C min^{-1}. Electrical contact and insulation were carried out as described in Section 2.2.1.

2.3. Photoanode characterization

To determine the band gap of the studied photocatalysts diffuse reflectance spectroscopy was performed using a LAMBDA 365 UV/Vis Spectrophotometer (PerkinElmer) equipped with an integrating sphere. The Kubelka- Munk function was calculated and the band gap values were obtained from the Tauc plot [34]. Indirect transition was assumed for both P25 and WO_3 to obtain the band gap energies [17,35]. To estimate the fraction of radiation absorbed, diffuse transmittance and reflectance of the photoanodes was measured from 200 to 700 nm with a scan rate of 5 nm s^{-1}. The methodology previously reported by Zacarías et al. [36] was followed. Briefly, two light trappers and two PTFE reflectance standards were placed in the comparison and sample ports of the sphere to set up the 0% and 100% reflectance respectively. The transmittance of the sample was measured by placing the sample in the sample holder compartment with the two PTFE standards in the sample and comparison rear ports of the integrating sphere. On the other hand, when the reflectance of the sample was recorded, the sample was placed on the sample rear port while keeping the reflectance standard in the comparison rear port.

The crystal structure of the photocatalysts was determined using Raman spectroscopy. Measurements were performed with a Renishaw Micro Raman spectrometer fitted with a He-Ne laser emitting at 532 nm, using a 10 s exposure and 3 exposures.

The morphology of the prepared photoanodes was analyzed by scanning electron microscopy (SEM) using a Hitachi SU5000 FE-SEM operated with an accelerating voltage of 5 kV and high vacuum pressure of $\sim 10^{-8}$ bar. The SEM was coupled to a dispersive energy X-ray (EDX/EDS) analyzer used to study elemental composition of the samples.

2.4. Photoelectrochemical characterization

Photoelectrochemical characterization was carried out in a three-electrode set-up allowing irradiation of the photoanode. The counter electrode was a Pt paddle and the reference electrode was a saturated calomel electrode (SCE). All potential values presented herein are expressed vs SCE unless otherwise stated. A 0.1 M Na_2SO_4 aqueous solution was used as the electrolyte for all the electrochemical measurements. All the experiments were performed using an electrochemical workstation (AUTOLAB PGSTAT 30) and the cell was irradiated by a 450 W xenon lamp (Horiba Jobin Yvon FL-1039/40) equipped with an IR water filter. The spectral radiation intensity provided by the Xe lamp was measured by using a spectral radiometer (Ocean Optics B.V, Netherlands) and the spectrum is shown in the Supplementary information (Fig. S1).

Linear sweep voltammetry (LSV), chronoamperometry and spectral photocurrent response were measured to assess the photoanode performance. LSV tests were carried out from − 1.0 V to + 1.0 V at sweep rate of 5 mV s^{-1}. For chopped irradiation a chopper (Uniblitz) was used with an on/off frequency of 10 s. The current-time response was recorded at a fixed potential of + 1.0 V for 230 s under chopped irradiation with an initial dark period of 30 s. A monochromator (Horiba Jobin Yvon MicroHR) was used to determine the spectral photocurrent response and incident photon-to-current efficiency (IPCE). Measurements were performed at a fixed potential of + 1.0 V under chopped irradiation and the wavelength was adjusted from 270 to 500 nm in 10 nm intervals.

Electrochemical impedance spectroscopy (EIS) was recorded using the software Nova version 1.16. Measurements were performed using sinusoidal perturbation with an AC amplitude of 10 mV in the frequency range between 0.01 Hz and 100 kHz. The experiments were carried out in the dark and under irradiation, at an applied potential of + 0.9 V. Mott-Schottky plots were obtained from impedance spectra scanned in the dark with a voltage of 10 mV at a frequency of 1 kHz and the potential was swept from 0.0 to + 0.1 V. The space charge layer capacitance (C) at each potential (E) was determined by fitting each spectrum to the Randles circuit. Flat-band potentials (E_{FB}) were estimated from the x-intercept of the linear region slope of the resulting Mott–Schottky plots (C^{-2} vs applied potential) at $C^{-2} = 0$ [34]. The donor density can also be obtained from the slope of the linear region according to the following Mott-Schottky equation:

$$\frac{1}{C^2} = \frac{2}{\varepsilon\varepsilon_0 A^2 e N_d}\left(E - E_{FB} - \frac{kT}{e}\right) \quad (1)$$

where ε_0 is permittivity in vacuum, ε is the relative dielectric constant of the material (50 was assumed [16]), A represents the area of the electrode, e is the charge of 1 electron (1.6×10^{-19} C), N_d is the donor density, k the Boltzmann constant (1.38×10^{-23} J/K) and T absolute temperature.

2.5. EAP degradation of sulfamethoxazole and removal of MS-2

The activity of the photoanodes was evaluated on the electrochemically assisted photocatalytic degradation of sulfamethoxazole (SMX) and on the inactivation of MS2. Experiments were performed using a 30 mL quartz water-jacketed reactor with magnetic flea and stirrer. The cell had an inner diameter and inner height of 3.5 cm. A Pt electrode was used as counter electrode and the photoanodes ($\sim 1.5 \times 1.3$ cm^2) as working electrodes. The electrolyte was 0.1 M Na_2SO_4. A 1000 W Xe lamp was used as irradiation source coupled with AM 1.5 filter. The distance between the lamp and the reactor was 87 cm to prevent the cell from being irradiated with an excessive amount of UV photons that can cause the photolysis of the pollutant. An infrared filter (containing ultrapure water) was placed between the Xe lamp and the cell to absorb the infrared radiation and prevent the working solution from heating. The irradiance was measured using a spectral radiometer (Ocean Optics B.V, Netherlands) and the spectrum of the Xe lamp is shown in the Supplementary information (Fig. S2). The incident photon flux in the UV and the 200–480 nm regions were $3.92 \cdot 10^{-9}$ Einstein s^{-1} cm^{-2} and $3.46 \cdot 10^{-8}$ Einstein s^{-1} cm^{-2} respectively. That way the UV incident radiation was similar to that previously in other studies [37]. The temperature of the cell was $\sim$ 25 °C.

Prior to the experiments a stock solution of 2 g L^{-1} of sulfamethoxazole was prepared in methanol. In a usual experiment, a certain volume of the stock solution was spiked in 30 mL of 0.1 M Na_2SO_4 to obtain an initial concentration of 10 mg L^{-1}, and the mixture was poured into the cell where it was continuously stirred. The electrodes were placed in the reactor which was stirred for 30 min in the dark to attain adsorption equilibrium. During the dark period the Xe lamp was switched on to let it stabilize. After stirring for 30 min, a sample was withdrawn, the desired cell potential was applied with a power supply and the reactor was exposed to the radiation. Air was continuously bubbled into the solution with an air blower. Samples were taken out every 15 min for the first hour and then every 30 min until the end of the reaction. The optimum applied cell potential was determined by sweeping the potential from 0 V to 1.5 V, with a step of 0.1 V, in dark and under irradiation and measuring the current response with a multimeter. The optimum potential was chosen as the applied potential at which the photocurrent density, the difference between the current response under irradiation and in the dark, reached a plateau.

Sulfamethoxazole concentration was detected and quantified by using an HPLC system (Agilent Technologies Series 1100) equipped with a UV detector and an analytical column Luna C18 (4.6 mm × 150 mm, 3 μm, Phenomenex). The injection volume was 100 μL and the detection wavelength was 267 nm. A gradient method was used: from 95/5 (v/v) of formic acid (25 mM)/acetonitrile to 20/80 (v/v) of formic acid (25 mM)/acetonitrile after 13 min and back to 95/5 (v/v) of formic acid (25 mM)/acetonitrile after 16 min, with a flow rate of 1 mL min^{-1}.

For MS2 inactivation experiments, the applied cell potential was 1.3 V (optimum potential determined in Section 3.4) with the semiconductor electrode as the anode. Three aliquots were taken out for each reaction time and MS2 was analyzed following the double-layer agar method [38]. For each photoanode, MS2 inactivation experiments were conducted in triplicate. A glycerol stock solution of MS2 bacteriophage (ATCC 15597-B1) kept frosted at − 80 °C (with an initial concentration of 10^{12} PFU mL^{-1}) and its *Escherichia coli* host (ATCC 15597) obtained from ATCC® were used. MS2 was spiked into the electrolyte getting an initial concentration of 10^6 PFU mL^{-1}. The averaged values and standard deviations were used for data analysis.

The overnight culture of the *E. coli* host was prepared from a glycerol master stock solution stored at − 80 °C. The *E. coli* host (from stock solution) was sowing in a Chromocult® Coliform Agar (Merck) plate incubated at 36 ± 2 °C for 21 ± 3 h. A single blue colony from the Chromocult plate was transferred to 15 mL of Tryptone Soya Broth (TSB, Oxoid) falcon tube that was incubated at 36 ± 2 °C for 12 h in a shaker incubator (200 rpm). The suspension was centrifuged at 4000 rpm for 5 min. The supernatant was suspended with phosphate borate saline (PBS) solution (Oxoid) to obtain an *E. coli* host concentration of 10^{12} CFU mL^{-1}.

For MS2 detection and enumeration, 1 mL of sample and 100 μL of *E. coli* host (from the overnight culture) were poured into a Bijou tube with melted Sloppy Agar, which was prepared with TSB and Agar Bacteriological No. 1 (Oxoid). The content of the Bijou tube was poured onto a Tryptone Soya Agar (TSA) plate (Oxoid). Petri dishes were

incubated at 36 ± 2 °C for 21 ± 3 h and lytic plaques were enumerated as MS2. Positive controls were performed to ensure stability of MS2 solution during the experimental time by taking samples of the working solution with MS2 before the EAP was applied, kept in the dark (covered by opaque foil) at room temperature and finally plated twice, at the beginning and at the end of the experimental time. The negative controls were plated from the following samples without MS2: PBS, *E. Coli* host, MS2 working solution and electrolyte to ensure no material, virus and host contamination. In addition, controls applying + 1.3 V in the dark (called 'electrochemical') and the photocatalytic removal of MS2 without any applied potential (called 'photocatalytic') were performed for each electrode sample.

3. Results and discussion

3.1. Physicochemical characterization of WO_3

In Fig. 1 SEM images of WO_3 and P25 electrodes are shown. Vertically oriented plate-like WO_3 structures were grown on the FTO glass (Fig. 1**A and B**). For the WO_3 synthesized hydrothermally at 180 °C for 3 h, the vertically grown layer of brick-like nanostructures was uniform and the nanoplates thickness ranged 40–300 nm. For the sample of WO_3 synthesized at 120 °C for 12 h the nanoplates were more homogeneous and the thickness varied between 70 and 250 nm. For the latter synthesis conditions the nanoplates showed fewer edges and boundaries compared to the nanostructures obtained at 180 °C and 3 h. These nanostructures have been reported to exhibit higher photocatalytic activity [12,39]. They can expose highly reactive facets and shorten the charge diffusion length. In Fig. 1**C** the SEM image of the P25 photoanode is shown. It can be noted that the coating is made of agglomerates of smaller P25 nanoparticles, giving rise to interparticle spaces. The thickness of the coatings was also measured using SEM and the images can be seen in Fig. S3. A significant difference between WO_3 and P25 coatings was observed. In both images the thicknesses were uniform, but whereas the thickness of WO_3 coating was around 0.5 μm, that of the P25 film was close to 50 μm. EDX analysis was also performed to analyze the chemical composition of the samples (Fig. 1**D and E**). As expected only O and W (Sn in Fig. 1D comes from the FTO) for the WO_3 and only O and Ti were detected for P25 photoanodes. The atomic ratio of O to W is 2.7, which indicates oxygen deficiency [29].

Diffuse reflectance was performed and the optical band gap energies of the photocatalysts coated on FTO was estimated using the Tauc plots (Fig. 2). From the plot, band gap values of 2.7 for WO_3 and 3.3 eV for P25 films were calculated. These values are in agreement with those

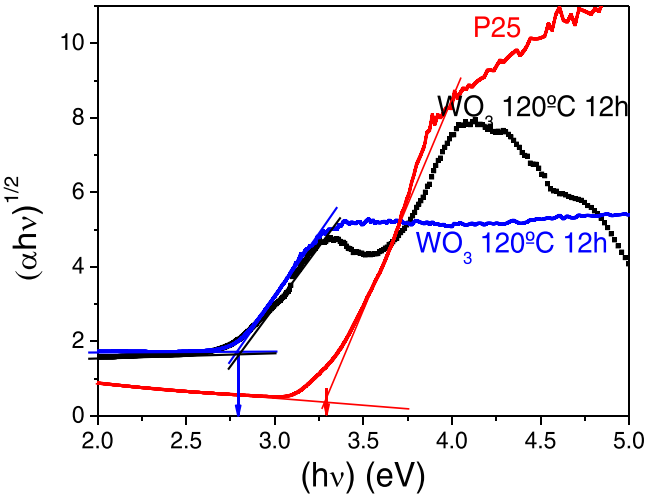

Fig. 2. Tauc plot used to estimate the band gap values.

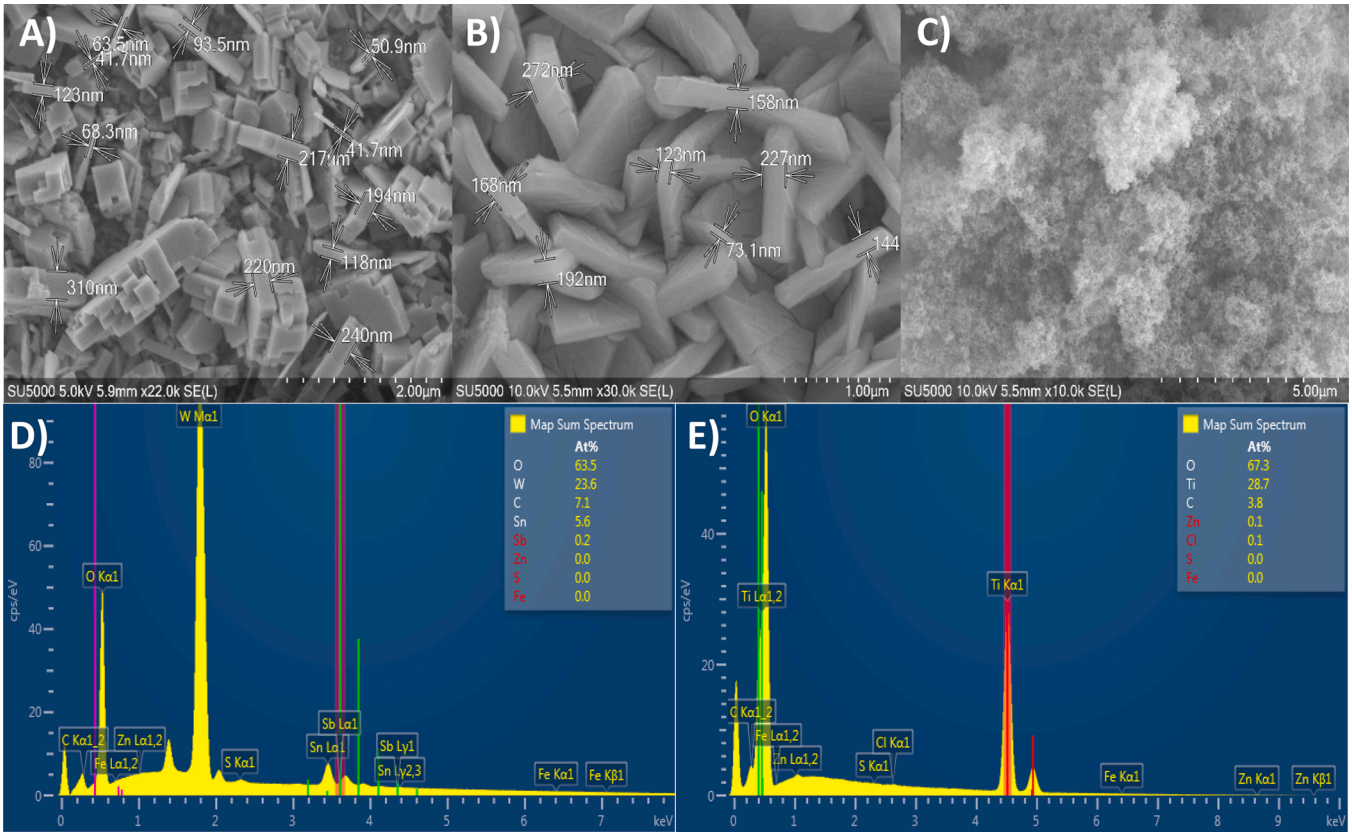

Fig. 1. SEM images of WO_3 180 °C 3 h (A), WO_3 120 °C 12 h (B) and P25 (C). EDX spectra of WO_3 120 °C 12 h (D) and P25 (E).

reported previously in the literature. The band gap values reported in other works are between 2.5–2.8 for WO_3 nanoplates [17,19] and 3.2–3.3 for P25 [40,41]. As expected, WO_3 band gap is lower than that of TiO_2 [10,41]. Hence, whereas P25 is only able to absorb radiation with a wavelength of up to ~ 400 nm (3.2 eV for Anatase and 3.0 eV for Rutile, it P25 is 80:20 Anatase: Rutile) WO_3 absorbs radiation up to 450 nm.

Raman spectra were recorded and analyzed to confirm the crystal structure of the TiO_2 and WO_3 photocatalysts (Fig. 3). P25 was a mixture of anatase (A) and rutile (R), giving eight Raman-active modes in the vibrational spectrum at 144 ($E_g(A) + B_{1\,g}(R)$), 195 ($E_g(A)$), 399 ($B_{1\,g}(A)$), 447 ($E_g(R)$), 519 ($A_{1\,g}(A) + B_{1\,g}(A)$), 639 ($E_g(A) + A_{1\,g}(R)$) and 806 cm^{-1} ($B_{2\,g}(R)$) [42]. Regarding WO_3 spectra, well defined peaks were detected at 72, 134 and 184 cm^{-1}, due to the lattice vibrations from the $(W_2O_2)_n$ chains of WO_3 [43,44]. The bands at 272 and 322 cm^{-1} correspond to O-W-O bending modes of the bridging oxygen, whereas those identified at 711 and 806 cm^{-1} were ascribed to O-W-O stretching modes [45,46]. These bands can be indexed to the monoclinic WO_3 structure [43–46]. The fact that there are several bands between 70 and 100 cm^{-1} due to lattice vibrations confirms the monoclinic phase as it is less asymmetric than the orthorhombic phase [44]. However, a small shoulder at 640 cm^{-1} could be observed in the spectrum of WO_3 120 °C 12 h. This band O-W-O was attributed to the stretching vibration of the bridging oxygen in the residual hydrated WO_3, so this sample did not only consist of a monoclinic phase [45].

3.2. Calculation of absorbed radiation by the photoanodes

The spectral local surface rate of photon absorption by the film ($e^{a,s}_{f,\lambda}$) was determined according to Manassero et al. [36,47], by performing a balance of the net radiation fluxes:

$$\left\langle e^{a,s}_{f,\lambda} \right\rangle = \left\langle q_{f,\lambda,in} \right\rangle_{A_{Cat}} - \left\langle q_{f,\lambda,tr} \right\rangle_{A_{Cat}} - \left\langle q_{f,\lambda,\ rf} \right\rangle_{A_{Cat}} = \left\langle q_{f,\lambda,in} \right\rangle_{A_{Cat}} \cdot \alpha_{f,\lambda} \quad (2)$$

where $\left\langle q_{f,\lambda,in} \right\rangle_{A_{Cat}}$, $\left\langle q_{f,\lambda,tr} \right\rangle_{A_{Cat}}$ and $\left\langle q_{f,\lambda,rf} \right\rangle_{A_{Cat}}$ are the surface average of the incident, transmitted and reflected radiation fluxes by the photocatalyst, respectively. Thus, the average surface rate of photon absorption for polychromatic radiation can be obtained from the spectral incident radiation flux and the spectral fraction of radiation absorbed ($\alpha_{f,\lambda}$):

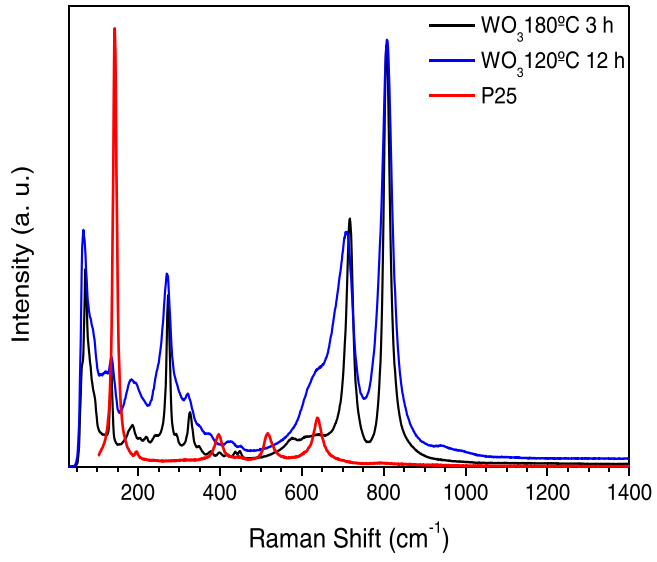

Fig. 3. Raman spectra of WO_3 180 °C 3 h, WO_3 120 °C 12 h and P25.

$$\left\langle e^{a,s}_{f,\lambda} \right\rangle = \left\langle q_{fg,\lambda,in} \right\rangle_{A_{Cat}} \cdot \alpha_{f,\lambda} \cdot T_{g,\lambda} \quad (3)$$

$$\alpha_{f,\lambda} = 1 - T_{f,\lambda} - R_{f,\lambda} \quad (4)$$

where $\left\langle q_{fg,\lambda,in} \right\rangle_{A_{Cat}}$ represents the spectral radiation flux that reaches the surface of the coated glass and $T_{g,\lambda}$ is the transmittance of the FTO glass to account for the radiation absorbed or reflected by the FTO glass. The spectral fraction of radiation absorbed ($\alpha_{f,\lambda}$) is calculated from the spectral transmittance ($T_{f,\lambda}$) and reflectance ($R_{f,\lambda}$) of the photocatalyst coating. $T_{f,\lambda}$ and $R_{f,\lambda}$ can be computed from diffuse reflectance (R_λ) and transmittance (T_λ) values of the coated (*fg*) and bare FTO glass (*g*) [36,47] according to the following expressions:

$$R_{f,\lambda} = \frac{R_{fg,\lambda} T_{g,\lambda}^{\ 2} - T_{fg,\lambda}^{\ 2} R_{g,\lambda}}{T_{g,\lambda}^{\ 2} - T_{fg,\lambda}^{\ 2} R_{g,\lambda}^{\ 2}} \quad (5)$$

$$T_{f,\lambda} = \frac{T_{fg,\lambda}}{T_{g,\lambda}} \left(1 - R_{f,\lambda} R_{g,\lambda}\right) \quad (6)$$

In Fig. S4 the fraction of absorbed radiation ($\alpha_{f,\lambda}$) by the different photocatalyst coatings are shown. It could be noted that $\alpha_{f,\lambda}$ was over 0.9 at 300 nm and then decreases until it reaches a steady value at wavelengths above that correspond to the band gap. By comparing the fraction of radiation absorbed obtained for the different photocatalysts, it was always lower for P25 even though the coating was much thicker. The values estimated here (0.86) agree with the values of α_f at 350 nm for P25 films previously reported (0.906) [36]. However, $\alpha_{f,\lambda}$ values for WO_3 remains over 0.8 up to 400 nm.

3.3. Photoelectrochemical characterization

The photoelectrochemical behavior of the prepared photoanodes was studied by performing linear sweep voltammetry (LSV) and chopped chronoamperometry under back-face irradiation. The main results are shown summarized in Fig. 4. Under back-face irradiation most of the electron-hole pairs are generated near the photocatalyst-FTO contact. Thus, photogenerated electrons are quickly collected at the supporting FTO electrode whereas holes will be trapped at the semiconductor-electrolyte interface on individual platelets of the photoanode to be transferred [10]. In Fig. 4**A** the voltammograms for the WO_3 and P25 photoanodes are shown. They were recorded from − 1.0 V to + 1.0 V under chopped irradiation. The photocurrent produced by WO_3 180 °C 3 h and WO_3 120 °C 12 h was far greater than the obtained with P25, 98.13, 140.27 and 12.05 μA cm^{-2} at + 1.0 V. Unfortunately, these results cannot be directly compared to those published by other research groups due to different experimental parameters. Yang et al. [20] detected a photocurrent close to 2.25 mA cm^{-2} at + 1.0 V (Ag/AgCl) using WO_3 nanoplates grown on FTO, but the LSV was carried out in acid pH using a 500 W Xe lamp and the electrolyte concentration was 5 times higher. Li et al. [31] synthesized WO_3 nanoflakes on FTO by a hydrothermal method that gave 0.62 mA cm^{-2} at + 1.0 V (Ag/AgCl) (~ 1.23 V vs RHE). The higher photocurrent they reported might be due to the different synthesis method as a WO_3 was precoated on the FTO and the hydrothermal process was carried out only for 2 h. Also, their electrolyte concentration was 10 times higher. A similar photocurrent (0.6 mA cm^{-2} at ~ 1.5 V (RHE) near + 1.0 V (SCE) was also reported by Li et al. [19] when they used WO_3 synthesized hydrothermally on FTO and natural seawater as electrolyte. However, despite the fact that the photocurrent they reported was greater than the observed in this work, their IPCE values for WO_3 are close to the IPCE values found here (around 30%). Thus, the difference in the photocurrent measured during LSV between both studies must be due to the different experimental conditions. Regarding LSV of P25, Byrne et al. [48] reported a short circuit photocurrent density (photocurrent obtained without any external applied voltage) of 13 μA cm^{-2} using KCl as electrolyte, which

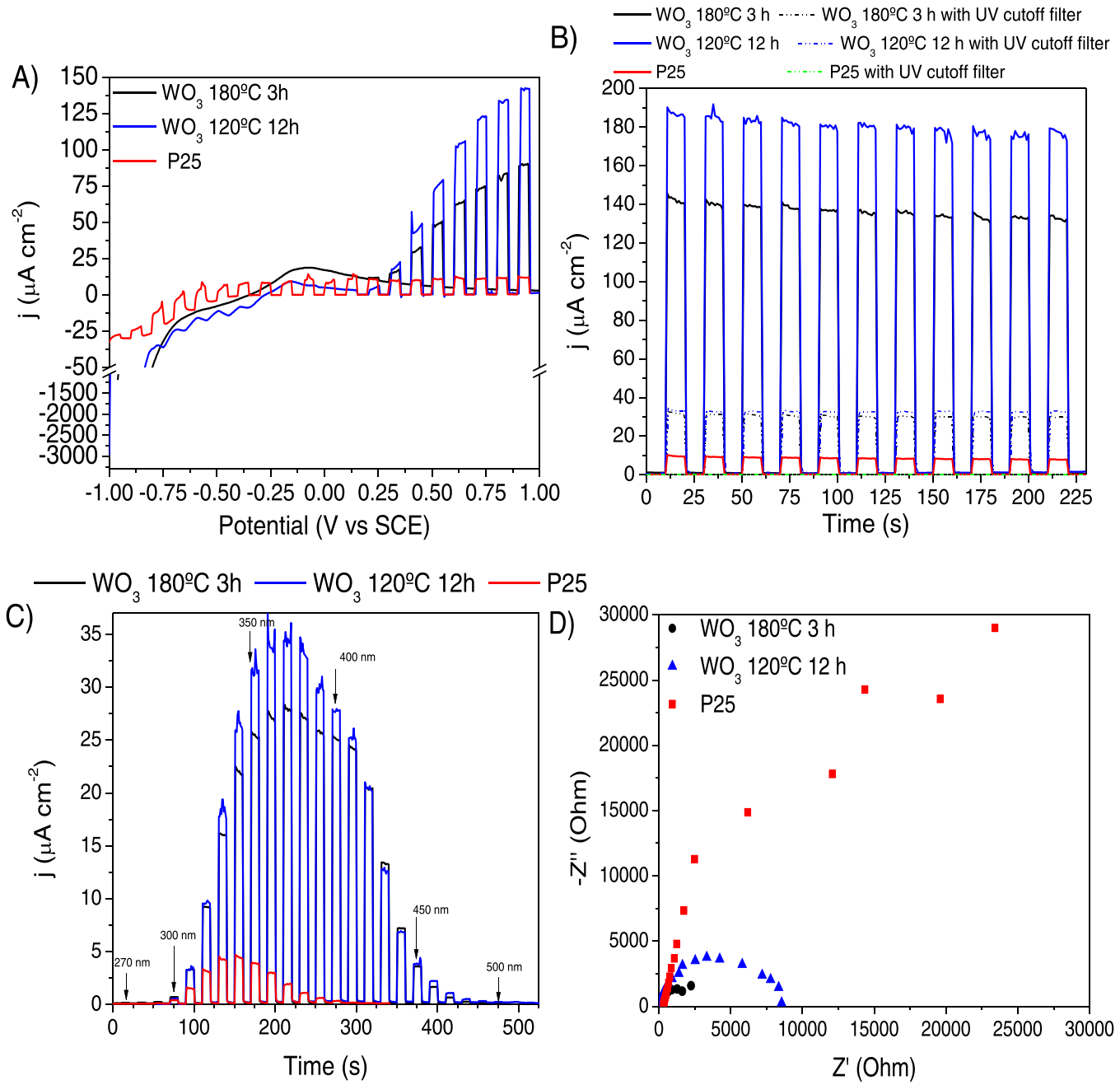

Fig. 4. (A) Linear sweep voltammetry (LSV) results, (B) Photocurrent density vs time curves chopped UV–vis light and using a UV cut-off filter, (C) spectral current response and (D) Nyquist plots measured under irradiation at 0.9 V vs SCE from 0.01 Hz to 100 kHz. In the experiments 0.1 M Na_2SO_4 aqueous solution was used as electrolyte, WO_3 180 °C 3 h, WO_3 120 °C 12 h and P25 were used as a photoanode and Pt as a cathode.

is identical to the value obtained in this work. The higher photocurrent exhibited by both photoanodes is ascribed to the plate-like morphology of the WO_3 which entails: 1) an increase of the surface area thanks to the vertically grown plate structures and the pores between them and 2) it provides a pathway for charges to migrate towards the conductive side of the substrate [19,20]. Hence, the morphology of the WO_3 helps reduce recombination of electron-hole pairs. On the other hand, the lower photocurrent for the P25 electrodes is due to the fact that they are mesoporous and in the absence of hole scavengers the holes are trapped within the film at the semiconductor-liquid interface and act as surface recombination sites [39].

In Fig. 4**B** the photocurrent response at + 1.0 V (SCE) under chopped irradiation every 10 s can be seen. Similar to what was observed before, the photocurrent produced by WO_3 was 16 times higher than the one observed with P25 (∼ 132 and ∼ 8 μA cm^{-2} respectively). Both photoanodes exhibited high photostability throughout the run and a quick response on light/dark cycles. To evaluate the photocurrent response at wavelengths greater than 400 nm a UV cut-off filter was placed between the lamp and the cell. Even under visible light WO_3 yielded a good photocurrent (∼ 30 μA cm^{-2}), even greater than the achieved by P25 under the whole spectrum. However, when the UV radiation was blocked, the photocurrent detected was negligible for the P25 photoanode. Fig. 4**C**, shows the spectral photocurrent response. Regardless of the wavelength, the photocurrent response was always higher for WO_3, with the highest peaks in the range between 340 and 420 nm for WO_3 and between 320 and 360 nm for P25. It is important to note the difference in the photocurrent at any wavelength above 300 nm and the higher spectral response of WO_3, which is able to produce measurable

photocurrents up to 490 nm. Hence, the good performance of WO_3 is not only due to the its morphology, but also because of its electronic properties [9].

EIS spectroscopy was measured to evaluate the charge transfer kinetics at the semiconductor electrolyte interface and the Nyquist plots are shown in Fig. 4**D**. Smaller semicircle radii were observed for WO_3 180 °C 3 h and WO_3 120 °C 12 h compared to P25, which indicates that the charge transfer resistance of WO_3 nanostructures is smaller than that of P25 [16,24,41].

Mott-Schottky measurements were conducted to confirm the type of semiconductor and estimate the flat-band potentials (E_{FB}) and donor density (N_D). In the Mott-Schottky plot, Fig. 5, a positive slope could be observed for both WO_3 samples typical for n-type semiconductors [34]. From the x-intercept of the Mott-Schottky plot the values of the flat-band potentials were + 0.22 V vs SCE and + 0.05 V vs SCE (+ 0.83 V and + 0.66 V vs RHE) for WO_3 180 °C 3 h and WO_3 120 °C 12 h electrodes. A negative shift of the E_{FB} has previously been reported to be beneficial for the EAP process, as more positive values of the flat-band potential decrease the bending of band edges [49]. From the optical band gap measurements, we can calculate that the valence band potentials are close to + 2.92 V vs SCE (+ 3.53 V vs RHE) for WO_3 180 °C 3 h and + 2.75 V vs SCE (+ 3.36 V vs RHE) for the WO_3 120 °C 12 h electrodes. From the slope in the linear region the N_D were estimated according to Eq. (1). The estimated N_D values were $3.38 \cdot 10^{19}$ and $5.0 \cdot 10^{19}$ cm^{-3} for WO_3 180 °C 3 h and WO_3 120 °C 12 h electrodes, respectively. The increase of the charge carrier concentration for WO_3 120 °C 3 h can be attributed to a higher amount of oxygen vacancies in the WO_3 lattice [31], which can act as electron traps, favouring electron/hole separation [29,31]. This was reported by Liu et al. [10] where they synthesized WO_3 and oxygen-deficient WO_{3-x} nanoplate array films and estimated the concentration of N_D for each of them. N_D values for WO_{3-x} were more than one order of magnitude larger than for WO_3. They proposed that the oxygen deficiencies allowed an easier electron transfer at the photoanode/electrolyte interface since the negative shift of the E_{FB}, and therefore of the Fermi level, leads to an enhanced electric field in the space charge layer and lower space charge layer that improves electron/hole separation.

The incident photon-to-current efficiency (IPCE) or external quantum efficiency (EQE) was calculated at a fixed potential of 1 V vs SCE (Fig. 6**A**). The IPCE is the ratio of the photocurrent density obtained to the rate of incident photons of a certain wavelength [34]. It considers the efficiency of electron-hole generation over the number of incident photons on the cell (η_{h^+/e^-}), charge transport efficiency ($\eta_{transport}$) and the efficiency of interfacial charge transfer ($\eta_{interface}$) [50]. The IPCE is calculated using the following equation:

$$IPCE(\lambda) = EQE(\lambda) = \frac{|j_{ph}\ (mA/cm^2)| \cdot hc\ (V \cdot nm)}{P_\lambda\ (mW/cm^2) \cdot \lambda\ (nm)} \quad (7)$$

where j_{ph} is the photocurrent density, h represents the Planck's constant, c is the speed of light, P_λ is the power intensity of the monochromatic light and λ is the wavelength of the monochromatic light. IPCE values indicated the higher performance of the WO_3 photoanode to turn incident radiation into current. The maximum IPCE value (29%) was obtained at 340 nm for WO_3 whereas the peak for P25 was detected at 330 nm (6.4%). The values for WO_3 hydrothermally grown on FTO are in accordance with those reported previously by Li et al. [19] although the values calculated for them are slightly lower. This is probably due to a lower reaction time of the hydrothermal process since they carried it out for only 1 h instead of 12 h. On the other hand, the IPCE values estimated here are three times greater than those reported by Li et al. [31] (near 10% at 360 nm). The difference is attributed to the different synthesis parameters as they precoated the FTO glass with WO_3 seed prior to the hydrothermal reaction. As a result, they obtained thinner nanoflakes (thickness between 20 and 30 nm) and with a greater overall film thickness (~ 2 μm).

Similarly, the Absorbed Photon to Current conversion Efficiency (APCE) or internal quantum efficiency (IQE) was determined at a fixed potential of 1 V vs SCE (Fig. 6**B**). The APCE is the ratio of the photocurrent density obtained to the rate of absorbed photons of a certain wavelength. This parameter provides information concerning the charge transport efficiency ($\eta_{transport}$) and the efficiency of interfacial charge transfer ($\eta_{interface}$) [34,51]. It can be calculated using the following equation:

$$APCE(\lambda) = IQE(\lambda) = \frac{|j_{ph}\quad (mA/cm^2)\,| \cdot 6.24 \cdot 10^{18} \frac{electrons}{C}}{\left\langle e_{f,\lambda}^{a,s} \right\rangle\ (photons \cdot cm^{-2} \cdot s^{-1})} \quad (8)$$

where j_{ph} is the photocurrent density and $\left\langle e_{f,\lambda}^{a,s} \right\rangle$ is the spectral average surface rate of photon absorption (described in Section 3.2). Values of the APCE were only calculated for wavelengths above 300 nm as at lower wavelengths the FTO transmittance is so low that leads to very low surface rates of photon absorption, and therefore to APCE values higher than 100%. It is important to note that the APCE is null at around 490 nm for WO_3 and 400 nm for P25, which agrees with their band gap values. The APCE values were always greater for WO_3 (50% at 360 nm) than for P25 (5.9% at 360 nm). On the other hand, smaller efficiencies were observed between the WO_3 180 °C 3 h and WO_3 120 °C 12 h photoanodes. Besides, while the APCE dropped exponentially for P25, the decline followed a linear trend in the case of both WO_3 photoanodes.

Hence, WO_3 has higher absorption radiation efficiency, charge separation and charge transfer efficiency, supporting the LSV and chronoamperometry results [19]. These results highlight the advantages of using nanostructures to increase the EAP performance e.g. they can expose highly reactive facets, increase surface area and shorten the charge diffusion length as well [12].

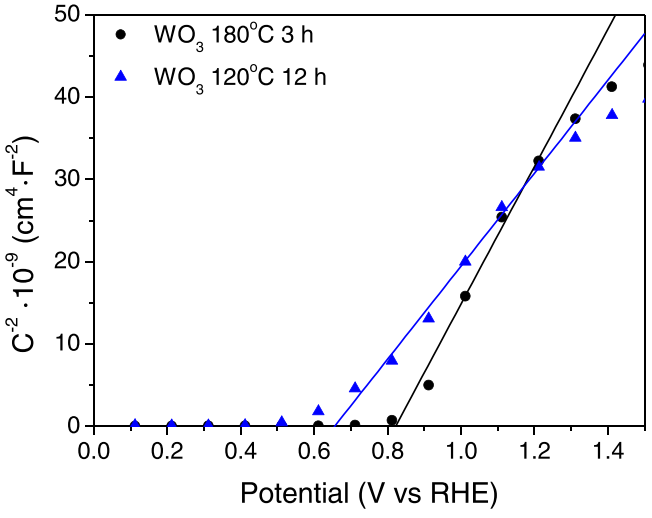

Fig. 5. Mott-Schottky plot of the WO_3 photoanodes.

3.4. Electrochemically assisted photodegradation of Sulfamethoxazole (SMX)

The activity of the WO_3 180 °C 3 h, WO_3 120 °C 12 h and P25 photoanodes was tested for the degradation of SMX. In Fig. 7**A**, the photocurrent response detected at different potentials for the different photoanodes is plotted. The selected applied potential was 1.3 V and 1.1 V for both WO_3 photoanodes and P25, respectively, to ensure the maximum photocurrent. The current response obtained in the dark and under irradiation for WO_3 180 °C 3 h, WO_3 120 °C 12 h and P25 electrodes can be found in the Supplementary information (Fig. S5). It can be noted that WO_3 120 °C 12 h (~ 370 μA cm^{-2} at 1.5 V) is able to reach

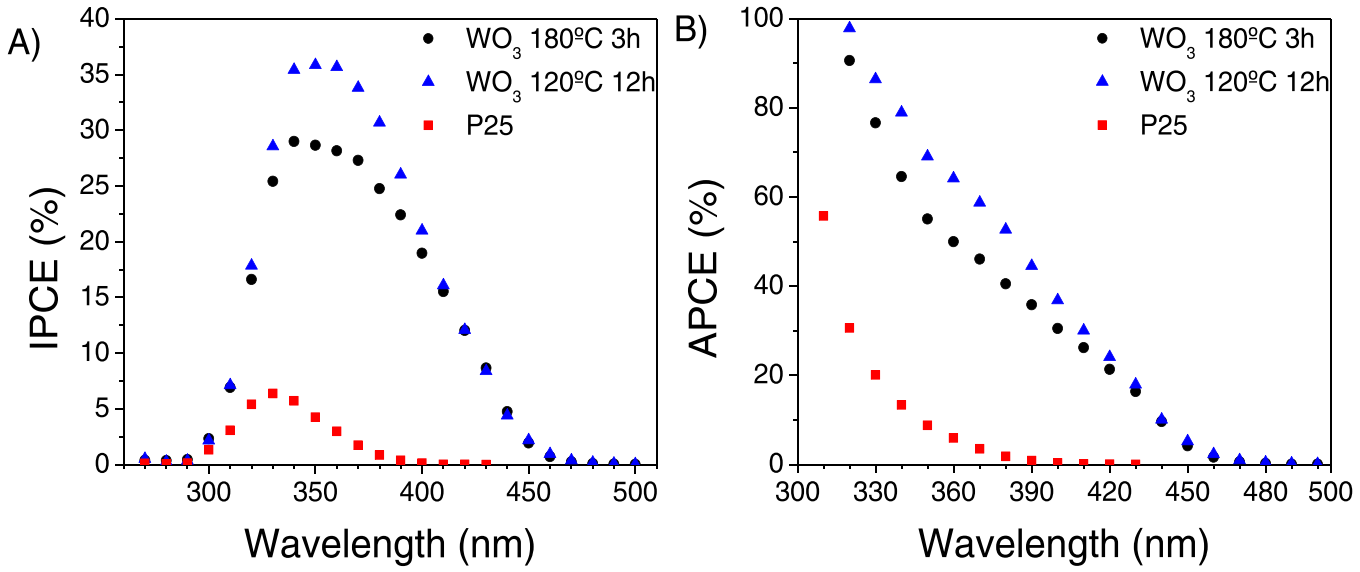

Fig. 6. (A) Incident photon-to-current efficiency (IPCE) and (B) Absorbed Photon to Current conversion Efficiency (APCE) spectra for the different prepared photoanodes.

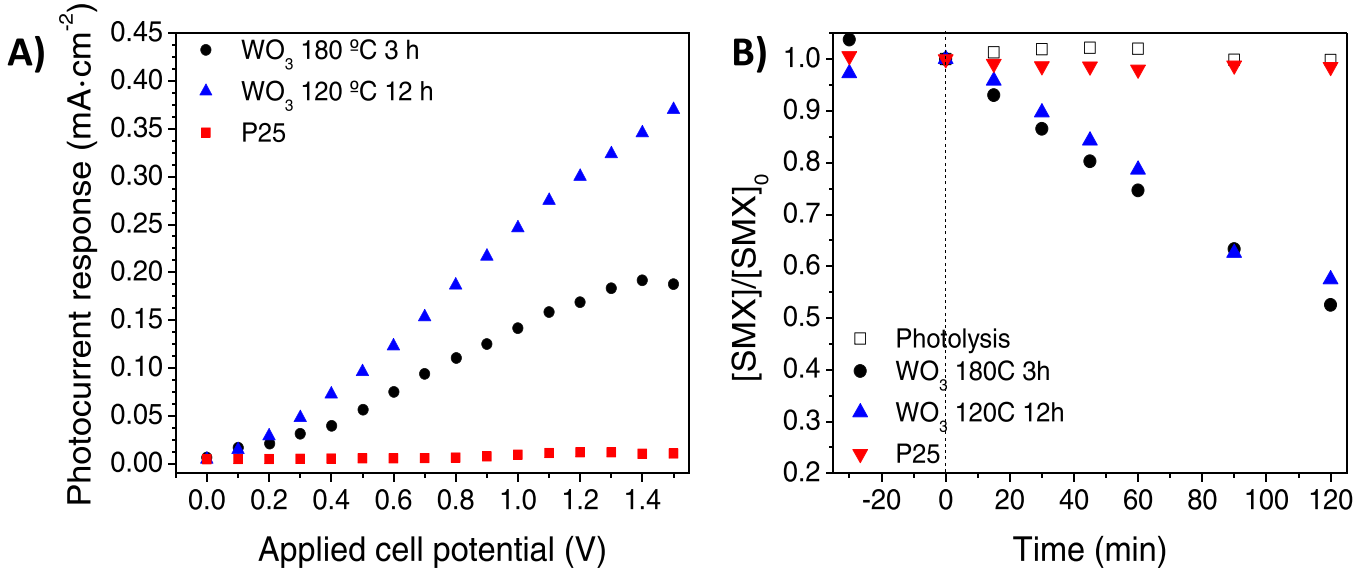

Fig. 7. Photocurrent densities obtained using WO_3 180 °C 3 h, WO_3 120 °C 12 h and P25 as a photoanode and Pt as a cathode (A). Evolution of sulfamethoxazole concentration (SMX) over electrochemically assisted photocatalytic (EAP) experiments under the following conditions (B): WO_3 180 °C 3 h, WO_3 120 °C 12 h and P25 were used as a photoanode and Pt as a cathode, $[SMX]_0 = 10$ mg L^{-1}, $V_T = 25$ mL, solar simulated light, I_0(200–480 nm) = 86 W m^{-2},applied potential = 1.3 V and 1.1 V for WO_3 and P25, respectively, and 0.1 M Na_2SO_4 in ultrapure water.

photocurrent values twice as high compared to WO_3 180 ºC 3 h ($\sim$ 188 μA cm^{-2} at 1.5 V). However, the photocurrent obtained with P25 ($\sim$ 10 μA cm^{-2} at 1.5 V) is negligible compared to WO_3 180 °C 3 h and WO_3 120 °C 12 h, which are $\sim$ 188 μA cm^{-2}, and $\sim$ 370 μA cm^{-2} at 1.5 V, respectively.

Regarding SMX degradation, all the blank experiments (photolysis, dark plus applied potential and photocatalytic experiments) are shown in Fig. 7**B** and in the Supplementary information (Fig. S5). Regardless of the photoanode, no SMX degradation was observed during the photolytic and photocatalytic processes and only a small conversion (< 10%) was observed for WO_3 180ºC 3 h under EC in the dark. It is noteworthy that P25, one of most effective reported photocatalyst (in suspension) for the degradation of pollutants in water, only attained a very little degradation via electrochemically assisted photocatalysis. The low efficiency obtained for P25 can be attributed to the mass transfer limitations when the photocatalyst is immobilized since the transport of the pollutant within the mesoporous layer is diffusion controlled [52, 53]. These results agrees with those published by Dale et al. [39] and Waldner et al. [54], which observed negligible effect of the applied potential for the removal of phenol and 4-chlorophenol by P25, respectively. This is attributed to the porous and disordered film formed upon immobilizing P25, which presents a high number of particle boundaries that are detrimental for the electron transfer and enhance electron/hole recombination [39].

By comparing the EAP degradation results (Fig. 7**B**), it could be observed that the conversion of SMX reached by WO_3 180 °C 3 h and WO_3 120 °C 12 h was almost 50%, even though the geometrical area of the WO_3 120 °C 12 h photoanode was 1.33 smaller than the one of WO_3 180 °C 3 h. The initial surface degradation rates averaged over the geometrical area of the photoanode ($\langle -r_{SMX}(x,t_0)\rangle_{A_{Cat}}$) were calculated

assuming zero order kinetics according to the following equation and the values are shown in Table 1.

$$\langle -r_{SMX}(x,t_0)\rangle_{A_{Cat}} = -\varepsilon_L \frac{V_T}{A_{Cat}} \lim_{t\to 0} \frac{\Delta C_{SMX}(t)}{\Delta t} \quad (9)$$

Where ε_L is the liquid hold-up ($\varepsilon_L \cong 1$), C_{SMX} represents the molar concentration of sulfamethoxazole, S_{Cat} is the geometrical surface area of the photoanode and V_T is the total volume of the working solution.

WO_3 120 °C 12 h yielded the fastest initial degradation rate (3.6×10^{-6} mmol cm^{-2} min^{-1}) followed by WO_3 180 °C 3 h (1.7×10^{-6} mmol cm^{-2} min^{-1}) and P25 (2.7×10^{-7} mmol cm^{-2} min^{-1}). These results follow the same sequence as the photocurrent response measured for the different photoanodes. Thus, the activity results highlight the relatively high performance of the WO_3 nanostructures, in agreement with the advantages previously mentioned i.e., increased of the surface area due to the morphology and structure of the WO_3, absorption of radiation up to 480 nm, and improved charge migration and charge transfer. For the P25 electrodes, there is little effect of the applied bias on photocurrent and charge recombination is favored because of the particle boundaries [39].

To check the feasibility of using WO_3 nanoplates for real applications, its reusability was tested for the degradation of sulfamethoxazole by performing five consecutive cycles (Fig. 8). To carry out the experiments WO_3 120 °C 12 h was selected as it exhibited the greatest degradation rate. It could be noted that the photoanode maintained the same performance over the cycles without noticeable decrease in the sulfamethoxazole conversion, reaching values around 37%. The stability of the photoanode might result from the relatively low applied potential in the EAP process.

3.5. Electrochemically assisted photoinactivation of MS2

MS2 bacteriophage is recommended by the WHO as a UV disinfection resistant viral surrogate in their protocol for evaluation of household water treatment options [55]. The negative controls confirmed no contamination from the samples of PBS, *E. Coli* host, MS2 working solution and electrolyte. As for the other control experiments, applying a cell potential of 1.3 V (anode potential ~ 1.2 V vs SCE) in the dark (EC) and the photocatalysis (without applying potential, PC), were carried out with the electrodes and no significant reduction on the MS2 concentration was observed (Fig. 9). The logarithmic reduction profiles of the normalized MS2 concentration (initial concentration of MS2 was 10^6 PFU mL^{-1}) achieved with WO_3 180 ºC 3 h, WO_3 120 ºC 12 h and P25 are shown in Fig. 9.

MS2 removal kinetics were analyzed according to the Chick-Watson model, fitting the linear part of the decay to the following equation:

$$Log\left(\frac{N}{N_0}\right) = -k \cdot t \quad (10)$$

where N is the concentration of MS2 at time t (PFU mL^{-1}), N_0 initial concentration of MS2 (PFU mL^{-1}), k the kinetic constant (min^{-1}) and t treatment time.

Similar to the results obtained for the degradation of sulfamethoxazole, the fastest inactivation rates and greatest *k* were obtained with WO_3 120 °C 12 h (0.89 min^{-1}) followed by WO_3 180 °C 3 h (0.62 min^{-1}) and P25 (0.40 min^{-1}). It is accepted that owing to the simple structure of the capsid, such as greater integrity of the viral capsid and no dependence on viability on chemically fragile enzymes, MS2 is inactivated by denaturing the protein of the capsid, therefore requiring wavelengths shorter than 295 nm or •OH necessary to remove MS2 [56,57]. This can only be attained using radiation of wavelength below 295 nm or a process that produces •OH [56,57]. Therefore, these results clearly confirm that photo-electrochemical performance of the novel WO_3 photoanodes are able to produce more ROS than P25 as they attain higher MS2 inactivation rates. However, the difference between the removal rates observed for WO_3 and P25 photoanodes were smaller than the rates reported in Table 1. Whereas WO_3 120 °C 12 h was able to achieve a 5-log reduction in less than 6 min, it took 8 and 14 min for WO_3 180 °C 3 h and P25 to reach the same value, respectively. This smaller difference might be due to the electrostatic interactions between the positively charged photoanode and the MS2 bacteriophage, which is negatively charged (isoelectric point of MS2 = 3.9 [56,58]), that improves the use of •OH [57]. Hence, the results support that WO_3 nanostructures not only improve degradation of organic pollutants, but also allow faster inactivation rates of viruses. Horovitz et al. used a photocatalytic reactor membrane coated with N-doped TiO_2 to remove MS2 from water with different qualities. However, even after 2 h only a 4.8-log reduction was achieved. Regarding EAP, Cho et al. [57] used TiO_2 particles coated onto an indium tin oxide (ITO) electrode to remove MS2. The UV intensity of the incident radiation was 100 W m^{-2}. For an applied potential of 2 V a 4-log reduction was observed after 80 min. However, much faster removal of MS2 was reported by Cho et al. [13] when TiO_2 nanotube arrays were used as photoanode. The UV intensity was 25 W m^{-2} and they reached a 3-log reduction after 10 min when the applied potential was 1 V vs Ag/AgCl and using 0.1 M Na_2SO_4. However, their ratio of working volume (40 mL) to working area of the photoanode (9.5 cm^2) was 4.2, which is three times lower than the use in this work. Therefore, the results of these preliminary tests highlight a good performance of the WO_3 nanostructures and is an exciting area for future research given the global concern about viral transmission and the global need for sustainable water treatment and disinfection technologies.

Table 1
Surface degradation rates of sulfamethoxazole using different photoanodes.

Photocatalyst	Area (cm^2)	($-r_{0,SMX}$) (mmol L^{-1} min^{-1})	($-r_{0,SMX}$) (mmol cm^{-2} min^{-1})
WO_3 180 °C 18 h	2.40	$1.59 \cdot 10^{-4}$	$1.66 \cdot 10^{-6}$
WO_3 120 °C 12 h	1.80	$1.59 \cdot 10^{-4}$	$2.21 \cdot 10^{-6}$
P25	1.80	$1.98 \cdot 10^{-5}$	$2.74 \cdot 10^{-7}$

4. Conclusions

In this study WO_3 nanoplates were synthesized and directly grown on FTO using a hydrothermal method for the EAP removal of a CEC and bacteriophage MS2 for the first time.

The activity of the prepared photoanodes was evaluated on the degradation of sulfamethoxazole and inactivation of MS2 by electrochemically assisted photocatalysis. It could be observed faster degradation of SMX and removal of MS2 by WO_3 photoanodes compared to P25, almost 50% SMX-conversion within 2 h against nearly 0%, and three times faster for MS2. The better performance of the WO_3 nanostructures than P25 was attributed to several positive factors: increased surface area due to the morphology and structure of the WO_3 (shown by SEM) and absorption of radiation with wavelengths up to 480 nm (estimated through the band gap values); because of the WO_3 nanostructures, higher ratio of absorbed radiation to incident radiation are obtained for WO_3 compared to P25 (estimated as 1.14 times higher at 365 nm). At the same time, owing to the morphology, charges can migrate more easily along the longitudinal direction and be more easily transferred at the electrode/electrolyte interface (verified by the LSV, chronoamperometry and impedance spectroscopy), reducing electron/hole recombination as seen by the IPCE and APCE values, which, therefore, leads to higher photocurrents and production of ROS. However, the effect of the applied bias is insignificant for P25 films and charge recombination is favored because particle boundaries act as surface recombination sites, hence its lower activity. Lastly, the prepared WO_3 photoanodes showed high stability and durability, proving its suitability to be reused several times.

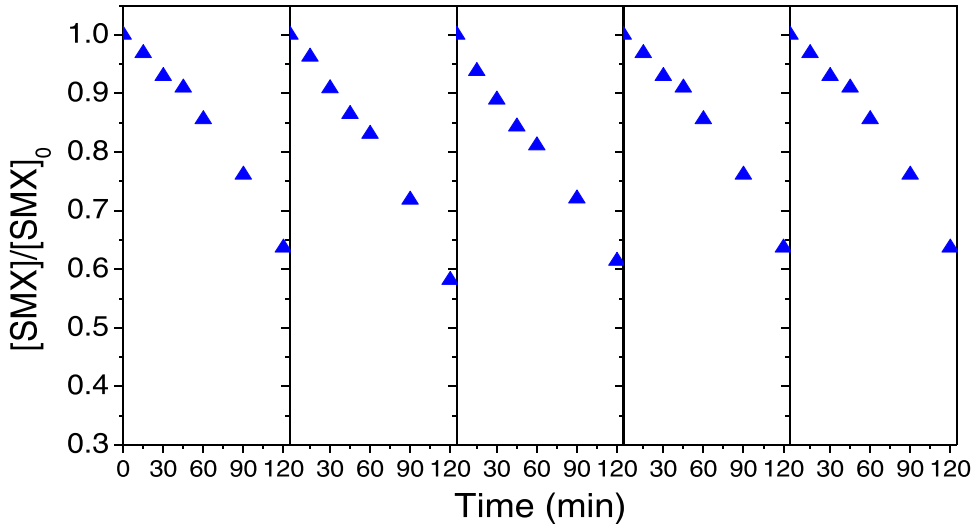

Fig. 8. Reusability of WO_3 120 °C 12 h for the degradation of sulfamethoxazole under the under the following conditions: Pt was used as a cathode, geometrical area of photoanode = 1.6 cm^2, $[SMX]_0$ = 10 mg L^{-1}, V_T = 25 mL, solar simulated light, I_0(200–480 nm) = 86 W m^{-2}, applied cell potential = 1.3 V and 0.1 M Na_2SO_4 in ultrapure water.

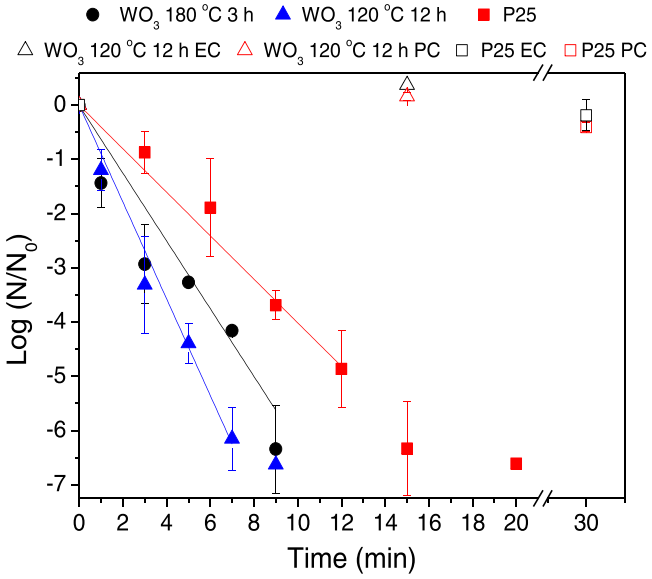

Fig. 9. EAP removal of MS2 obtained using WO_3 180 °C 3 h, WO_3 120 °C 12 h and P25 as a photoanode and Pt as a cathode. $[MS2]_0 = 10^7$ PFU mL^{-1}, V_T = 25 mL, solar simulated light, I_0(200–480 nm) = 86 W m^{-2}, applied potential = 1.3 V and 0.1 M Na_2SO_4 electrolyte. Lines represent the linear fittings to the Chick-Watson model.

CRediT authorship contribution statement

Alvaro Tolosana-Moranchel: Conceptualization, Methodology, Investigation, software, Writing – original draft, Writing – review & editing. **Natalia Pichel:** Methodology, Investigation, Writing – original draft. **Helen Lubarsky**: Methodology, Investigation, Writing – original draft. **John Anthony Byrne:** Supervision, Writing – original draft, Writing – review & editing, Funding acquisition. **Pilar Fernández-Ibañez:** Supervision, Writing – original draft, Writing – review & editing, Funding acquisition.

Declaration of Competing Interest

The authors declare that they have no known competing financial interests or personal relationships that could have appeared to influence the work reported in this paper.

Acknowledgements

The authors wish to thank the EU-India H2020 cooperation program for funding this work under the PANIWATER Project (RIA GA-820718) and GCRF UKRI for funding SAFEWATER (EP/P032427/1).

Appendix A. Supporting information

Supplementary data associated with this article can be found in the online version at doi:10.1016/j.jece.2022.107955.

References

[1] D. Akhil, D. Lakshmi, P. Senthil Kumar, D.V.N. Vo, A. Kartik, Occurrence and Removal of Antibiotics from Industrial Wastewater, Springer International Publishing, 2021, https://doi.org/10.1007/s10311-020-01152-0.
[2] E.P. Costa, M.C.V.M. Starling, C.C. Amorim, Simultaneous removal of emerging contaminants and disinfection for municipal wastewater treatment plant effluent quality improvement: a systemic analysis of the literature, Environ. Sci. Pollut. Res. (2021) 24092–24111, https://doi.org/10.1007/s11356-021-12363-5.
[3] K. O'Dowd, K.M. Nair, S.C. Pillai, Photocatalytic degradation of antibiotic-resistant genes and bacteria using 2D nanomaterials: what is known and what are the challenges? Curr. Opin. Green Sustain. Chem. 30 (2021), 100471 https://doi.org/10.1016/j.cogsc.2021.100471.
[4] B. Saba, S.W. Hasan, B.V. Kjellerup, A.D. Christy, Capacity of existing wastewater treatment plants to treat SARS-CoV-2. A review, Bioresour. Technol. Rep. 15 (2021), 100737, https://doi.org/10.1016/J.BITEB.2021.100737.
[5] D. Paul, P. Kolar, S.G. Hall, A review of the impact of environmental factors on the fate and transport of coronaviruses in aqueous environments, Npj Clean. Water 4 (2021), https://doi.org/10.1038/s41545-020-00096-w.
[6] I. Sirés, E. Brillas, Remediation of water pollution caused by pharmaceutical residues based on electrochemical separation and degradation technologies: a review, Environ. Int. 40 (2012) 212–229, https://doi.org/10.1016/j.envint.2011.07.012.
[7] J. Byrne, P. Dunlop, J. Hamilton, P. Fernández-Ibáñez, I. Polo-López, P. Sharma, A. Vennard, A review of heterogeneous photocatalysis for water and surface disinfection, Molecules 20 (2015) 5574–5615, https://doi.org/10.3390/molecules20045574.
[8] M. Pelaez, N.T. Nolan, S.C. Pillai, M.K. Seery, P. Falaras, A.G. Kontos, P.S. M. Dunlop, J.W.J. Hamilton, J.A. Byrne, K. O'Shea, M.H. Entezari, D.D. Dionysiou, A review on the visible light active titanium dioxide photocatalysts for environmental applications, Appl. Catal. B Environ. 125 (2012) 331–349, https://doi.org/10.1016/J.APCATB.2012.05.036.
[9] E. Kusmierek, Semiconductor electrode materials applied in photoelectrocatalytic wastewater treatment—an overview, Catalysts 10 (2020) 1–49, https://doi.org/10.3390/catal10040439.

[10] X. Liu, H. Zhou, S. Pei, S. Xie, S. You, Oxygen-deficient WO3-x nanoplate array film photoanode for efficient photoelectrocatalytic water decontamination, Chem. Eng. J. 381 (2019), 122740, https://doi.org/10.1016/j.cej.2019.122740.

[11] E. Kusmierek, Evaluating the effect of WO3 on electrochemical and corrosion properties of TiO2-RuO2-coated titanium anodes with low content of RuO2, Electrocatalysis 11 (2021) 555–566, https://doi.org/10.1007/s12678-020-00615-w.

[12] Y. Wang, M. Zu, X. Zhou, H. Lin, F. Peng, S. Zhang, Designing efficient TiO2-based photoelectrocatalysis systems for chemical engineering and sensing, Chem. Eng. J. 381 (2020), 122605, https://doi.org/10.1016/j.cej.2019.122605.

[13] K. Cho, S. Lee, H. Kim, H.E. Kim, A. Son, E. ju Kim, M. Li, Z. Qiang, S.W. Hong, Effects of reactive oxidants generation and capacitance on photoelectrochemical water disinfection with self-doped titanium dioxide nanotube arrays, Appl. Catal. B Environ. 257 (2019), 117910, https://doi.org/10.1016/j.apcatb.2019.117910.

[14] L. Yu, Z. Wang, L. Shi, S. Yuan, Y. Zhao, J. Fang, W. Deng, Photoelectrocatalytic performance of TiO2 nanoparticles incorporated TiO2 nanotube arrays, Appl. Catal. B Environ. 113–114 (2012) 318–325, https://doi.org/10.1016/j.apcatb.2011.12.004.

[15] J. Zhang, B. Tang, G. Zhao, Selective photoelectrocatalytic removal of dimethyl phthalate on high-quality expressed molecular imprints decorated specific facet of single crystalline TiO2 photoanode, Appl. Catal. B Environ. 279 (2020), 119364, https://doi.org/10.1016/j.apcatb.2020.119364.

[16] R.M. Fernández-Domene, R. Sánchez-Tovar, B. Lucas-granados, M.J. Muñoz-Portero, J. García-Antón, Elimination of pesticide atrazine by photoelectrocatalysis using a photoanode based on WO3 nanosheets, Chem. Eng. J. 350 (2018) 1114–1124, https://doi.org/10.1016/j.cej.2018.06.015.

[17] N. Li, H. Teng, L. Zhang, J. Zhou, M. Liu, Synthesis of Mo-doped WO3 nanosheets with enhanced visible-light-driven photocatalytic properties, RSC Adv. 5 (2015) 95394–95400, https://doi.org/10.1039/c5ra17098b.

[18] G.F. Cai, J.P. Tu, D. Zhou, L. Li, J.H. Zhang, X.L. Wang, C.D. Gu, The direct growth of a WO3 nanosheet array on a transparent conducting substrate for highly efficient electrochromic and electrocatalytic applications, CrystEngComm 16 (2014) 6866–6872, https://doi.org/10.1039/c4ce00404c.

[19] Y. Li, X. Wei, X. Yan, J. Cai, A. Zhou, M. Yang, K. Liu, Construction of inorganic-organic 2D/2D WO3/g-C3N4 nanosheet arrays toward efficient photoelectrochemical splitting of natural seawater, Phys. Chem. Chem. Phys. 18 (2016) 10255–10261, https://doi.org/10.1039/c6cp00353b.

[20] J. Yang, W. Li, J. Li, D. Sun, Q. Chen, Hydrothermal synthesis and photoelectrochemical properties of vertically aligned tungsten trioxide (hydrate) plate-like arrays fabricated directly on FTO substrates, J. Mater. Chem. 22 (2012) 17744–17752, https://doi.org/10.1039/c2jm33199c.

[21] M. José Martín de Vidales, L. Mais, C. Sáez, P. Cañizares, F.C. Walsh, M.A. Rodrigo, C. de A. Rodrigues, C. Ponce de León, Photoelectrocatalytic oxidation of methyl orange on a tio2 nanotubular anode using a flow cell, Chem. Eng. Technol. 39 (2016) 135–141, https://doi.org/10.1002/ceat.201500085.

[22] T. Bosserez, J. Rongé, J. van Humbeeck, S. Haussener, J. Martens, Design of compact photoelectrochemical cells for water splitting, Oil Gas Sci. Technol. – Rev. d'IFP Energ. Nouv. 70 (2015) 877–889, https://doi.org/10.2516/ogst/2015015.

[23] B.X. Lei, J.Y. Liao, R. Zhang, J. Wang, C.Y. Su, D. Bin Kuang, Ordered crystalline TiO2 nanotube arrays on transparent FTO glass for efficient dye-sensitized solar cells, J. Phys. Chem. C 114 (2010) 15228–15233, https://doi.org/10.1021/jp105780v.

[24] H. Wang, W. Liang, W. Zhang, D. Zhou, Photoelectric performance of TiO2 nanotube array film of highly transparent vs nontransparent on FTO glass, Mater. Sci. Semicond. Process. 71 (2017) 50–53, https://doi.org/10.1016/j.mssp.2017.07.005.

[25] M. Zelny, S. Kment, R. Ctvrtlik, S. Pausova, H. Kmentova, J. Tomastik, Z. Hubicka, Y. Rambabu, J. Krysa, A. Naldoni, P. Schmuki, R. Zboril, Tio2 nanotubes on transparent substrates: control of film microstructure and photoelectrochemical water splitting performance, Catalysts 8 (2018) 25, https://doi.org/10.3390/catal8010025.

[26] Š. Paušová, Š. Kment, M. Zlámal, M. Baudys, Z. Hubička, J. Krýsa, Transparent nanotubular TiO2 photoanodes grown directly on FTO substrates, Molecules 22 (2017) 775, https://doi.org/10.3390/molecules22050775.

[27] H. Kmentova, S. Kment, L. Wang, S. Pausova, T. Vaclavu, R. Kuzel, H. Han, Z. Hubicka, M. Zlamal, J. Olejnicek, M. Cada, J. Krysa, R. Zboril, Photoelectrochemical and structural properties of TiO2 nanotubes and nanorods grown on FTO substrate: comparative study between electrochemical anodization and hydrothermal method used for the nanostructures fabrication, Catal. Today 287 (2017) 130–136, https://doi.org/10.1016/j.cattod.2016.10.022.

[28] X. Jiang, Q. Lin, Y. Zhang, K. Dong, Y. Zhang, Y. Shi, TiO2 nanotube arrays: hydrothermal fabrication and photocatalytic activities, J. Mater. Sci. Mater. Electron. 28 (2017) 12509–12513, https://doi.org/10.1007/s10854-017-7073-5.

[29] F. Zheng, H. Lu, M. Guo, M. Zhang, Q. Zhen, Hydrothermal preparation of WO3 nanorod array and ZnO nanosheet array composite structures on FTO substrates with enhanced photocatalytic properties, J. Mater. Chem. C 3 (2015) 7612–7620, https://doi.org/10.1039/c5tc01125f.

[30] G. Zhang, W. Guan, H. Shen, X. Zhang, W. Fan, C. Lu, H. Bai, L. Xiao, W. Gu, W. Shi, Organic additives-free hydrothermal synthesis and visible-light-driven photodegradation of tetracycline of WO3 nanosheets, Ind. Eng. Chem. Res. 53 (2014) 5443–5450, https://doi.org/10.1021/ie4036687.

[31] W. Li, P. Da, Y. Zhang, Y. Wang, X. Lin, X. Gong, G. Zheng, WO3 nanoflakes for enhanced photoelectrochemical conversion, ACS Nano 8 (2014) 11770–11777, https://doi.org/10.1021/nn5053684.

[32] T.A. McMurray, J.A. Byrne, P.S.M. Dunlop, E.T. McAdams, Photocatalytic and electrochemically assisted photocatalytic oxidation of formic acid on TiO2 films under UVA and UVB irradiation, J. Appl. Electrochem. 35 (2005) 723–731, https://doi.org/10.1007/s10800-005-1397-1.

[33] T.A. McMurray, P.S.M. Dunlop, J.A. Byrne, The photocatalytic degradation of atrazine on nanoparticulate TiO2 films, J. Photochem. Photobiol. A Chem. 182 (2006) 43–51, https://doi.org/10.1016/j.jphotochem.2006.01.010.

[34] Z. Chen, T.G. Deutsch, H.N. Dinh, K. Domen, K. Emery, A.J. Forman, N. Gaillard, R. Garland, C. Heske, T.F. Jaramillo, A. Kleiman-Shwarsctein, E. Miller, K. Takanabe, J. Turner, Photoelectrochemical Water Splitting, 2013. ⟨https://doi.org/10.1007/978-1-4614-8298-7_5⟩.

[35] Z. DohŁeviĿ-MitroviĿ, S. StojadinoviĿ, L. Lozzi, S. AŝkrabiĿ, M. RosiĿ, N. TomiĿ, N. PaunoviĿ, S. LazoviĿ, M.G. NikoliĿ, S. Santucci, WO3/TiO2 composite coatings: structural, optical and photocatalytic properties, Mater. Res. Bull. 83 (2016) 217–224, https://doi.org/10.1016/J.MATERRESBULL.2016.06.011.

[36] S.M. Zacarías, M.L. Satuf, M.C. Vaccari, O.M. Alfano, Efficiency evaluation of different TiO2 coatings on the photocatalytic inactivation of airborne bacterial spores, Ind. Eng. Chem. Res. 51 (2012) 13599–13608, https://doi.org/10.1021/ie3009956.

[37] Á. Tolosana-Moranchel, A. Manassero, M.L. Satuf, O.M. Alfano, J.A. Casas, A. Bahamonde, TiO2-rGO photocatalytic degradation of an emerging pollutant: kinetic modelling and determination of intrinsic kinetic parameters, J. Environ. Chem. Eng. 7 (2019), 103406, https://doi.org/10.1016/j.jece.2019.103406.

[38] M.H. Adams, Bacteriophages, Interscience Publishers, New York, 1959.

[39] G. Dale, J. Hamilton, P. Dunlop, J. Byrne, Electrochemically assisted photocatalysis on anodic titania nanotubes, Curr. Top. Electrochem. 14 (2009) 89–97.

[40] A. Tolosana-Moranchel, J.A. Anderson, J.A. Casas, M. Faraldos, A. Bahamonde, Defining the role of substituents on adsorption and photocatalytic degradation of phenolic compounds, J. Environ. Chem. Eng. 5 (2017) 4612–4620, https://doi.org/10.1016/j.jece.2017.08.053.

[41] A. Tolosana-Moranchel, J.A. Casas, A. Bahamonde, L. Pascual, L.I. Granone, J. Schneider, R. Dillert, D.W. Bahnemann, Nature and photoreactivity of TiO2-rGO nanocomposites in aqueous suspensions under UV-A irradiation, Appl. Catal. B Environ. 241 (2019) 375–384, https://doi.org/10.1016/j.apcatb.2018.09.070.

[42] G. Luna-Sanguino, A. Ruíz-Delgado, A. Tolosana-Moranchel, L. Pascual, S. Malato, A. Bahamonde, M. Faraldos, Solar photocatalytic degradation of pesticides over TiO_2-rGO nanocomposites at pilot plant scale, Sci. Total Environ. 737 (2020), https://doi.org/10.1016/j.scitotenv.2020.140286.

[43] J.Y. Zheng, G. Song, J. Hong, T.K. Van, A.U. Pawar, D.Y. Kim, C.W. Kim, Z. Haider, Y.S. Kang, Facile fabrication of WO3 nanoplates thin films with dominant crystal facet of (002) for water splitting, Cryst. Growth Des. 14 (2014) 6057–6066, https://doi.org/10.1021/cg5012154.

[44] Y. Djaoued, S. Balaji, R. Brüning, Electrochromic devices based on porous tungsten oxide thin films, J. Nanomater. (2012) (2012), https://doi.org/10.1155/2012/674168.

[45] C. Santato, M. Odziemkowski, M. Ulmann, J. Augustynski, Crystallographically oriented mesoporous WO3 films: synthesis, characterization, and applications, J. Am. Chem. Soc. 123 (2001) 10639–10649, https://doi.org/10.1021/ja011315x.

[46] J. Díaz-Reyes, R. Castillo-Ojeda, M. Galván-Arellano, O. Zaca-Moran, Characterization of WO3 thin films grown on silicon by HFMOD, Adv. Condens. Matter Phys. (2013) (2013), https://doi.org/10.1155/2013/591787.

[47] A. Manassero, S.M. Zacarías, M.L. Satuf, O.M. Alfano, Intrinsic kinetics of clofibric acid photocatalytic degradation in a fixed-film reactor, Chem. Eng. J. 283 (2016) 1384–1391, https://doi.org/10.1016/J.CEJ.2015.08.060.

[48] J. Anthony Byrne, B.R. Eggins, S. Linquette-Mailley, P.S.M. Dunlop, The effect of hole acceptors on the photocurrent response of particulate TiO2 anodes, Analyst 123 (1998) 2007–2012, https://doi.org/10.1039/a803885f.

[49] M. Radecka, M. Rekas, A. Trenczek-Zajac, K. Zakrzewska, Importance of the band gap energy and flat band potential for application of modified TiO2 photoanodes in water photolysis, J. Power Sources 181 (2008) 46–55, https://doi.org/10.1016/j.jpowsour.2007.10.082.

[50] G.G. Bessegato, T.T. Guaraldo, J.F. de Brito, M.F. Brugnera, M.V.B. Zanoni, Achievements and trends in photoelectrocatalysis: from environmental to energy applications, Electrocatalysis 6 (2015) 415–441, https://doi.org/10.1007/s12678-015-0259-9.

[51] S. Giménez, J. Bisquert, Photoelectrochemical Solar Fuel Production: From Basic Principles to Advanced Devices, 2016, https://doi.org/10.1007/978-3-319-29641-8.

[52] C. Pablos, J. Marugán, C. Adán, M. Osuna, R. van Grieken, Performance of TiO2 photoanodes toward oxidation of methanol and E. coli inactivation in water in a scaled-up photoelectrocatalytic reactor, Electrochim. Acta (2017), https://doi.org/10.1016/j.electacta.2017.11.103.

[53] S. Malato, P. Fernández-Ibáñez, M.I. Maldonado, J. Blanco, W. Gernjak, Decontamination and disinfection of water by solar photocatalysis: recent overview and trends, Catal. Today 147 (2009) 1–59, https://doi.org/10.1016/J.CATTOD.2009.06.018.

[54] G. Waldner, J. Krýsa, J. Jirkovský, G. Grabner, Photoelectrochemical properties of sol-gel and particulate TiO2 layers, Int. J. Photoenergy 5 (2003) 115–122, https://doi.org/10.1155/S1110662×03000229.

[55] W.H. Organization, Evaluating Household Water Treatment Options: Health-based Targets and Microbiological Performance Specifications, 2011, p. 59.

[56] I. Horovitz, D. Avisar, E. Luster, L. Lozzi, T. Luxbacher, H. Mamane, MS2 bacteriophage inactivation using a N-doped TiO2-coated photocatalytic membrane

reactor: influence of water-quality parameters, Chem. Eng. J. 354 (2018) 995–1006, https://doi.org/10.1016/j.cej.2018.08.083.
[57] M. Cho, E.L. Cates, J.H. Kim, Inactivation and surface interactions of MS-2 bacteriophage in a TiO2 photoelectrocatalytic reactor, Water Res. 45 (2011) 2104–2110, https://doi.org/10.1016/j.watres.2010.12.017.
[58] A. Armanious, M. Aeppli, R. Jacak, D. Refardt, T. Sigstam, T. Kohn, M. Sander, Viruses at solid-water interfaces: a systematic assessment of interactions driving adsorption, Environ. Sci. Technol. 50 (2016) 732–743, https://doi.org/10.1021/acs.est.5b04644.